CM²

MAGAZINE

第 35 期

创刊词

　　海洋是生命的摇篮，是文明的纽带。地球上最早的生命诞生于海洋，海洋里的生命最终进化成了人类，人类的文化融合又通过海洋得以实现。人因海而兴。

　　人类对海洋的探索从未停止。从远古时代美丽的神话传说，到麦哲伦的全球航行，再到现代对大洋的科学钻探计划，海洋逐渐从人类敬畏崇拜幻想的精神寄托演变成可以开发利用与科学研究的客观存在。其中，上个世纪与太空探索同步发展的大洋科学钻探计划将人类对海洋的认知推向了崭新的纬度：深海（deep sea）与深时（deep time）。大洋钻探计划让人类知道，奔流不息的大海之下，埋藏的却是亿万年的地球历史。它们记录了地球板块的运动，从而使板块构造学说得到证实；它们记录了地球环境的演变，从而让古海洋学方兴未艾。

　　在探索海洋的悠久历史中，从大航海时代的导航，到大洋钻探计划中不可或缺的磁性地层学，磁学发挥了不可替代的作用。这不是偶然，因为从微观到宏观，磁性是最基本的物理属性之一，可以说，万物皆有磁性。基于课题组的学科背景和对海洋的理解，我们对海洋的探索以磁学为主要手段，海洋磁学中心因此而生。

　　海洋磁学中心，简称 CM^2，一为其全名"Centre for Marine Magnetism"的缩写，另者恰与爱因斯坦著名的质能方程 $E = MC^2$ 对称，借以表达我们对科学巨匠的敬仰和对科学的不懈追求。

　　然而科学从来不是单打独斗的产物。我们以磁学为研究海洋的主攻利器，但绝不仅限于磁学。凡与磁学相关的领域均是我们关注的重点。为了跟踪反映国内外地球科学特别是与磁学有关的地球科学领域的最新研究进展，海洋磁学中心特地主办 CM^2 Magazine，以期与各位地球科学工作者相互交流学习、合作共进！

　　"海洋孕育了生命，联通了世界，促进了发展"。21 世纪是海洋科学的时代，由陆向海，让我们携手迈进中国海洋科学的黄金时代

目 录

岩石磁学演绎

第 25 章　RPI 曲线长啥样?

　　RPI 最大的优点就是它的连续性。

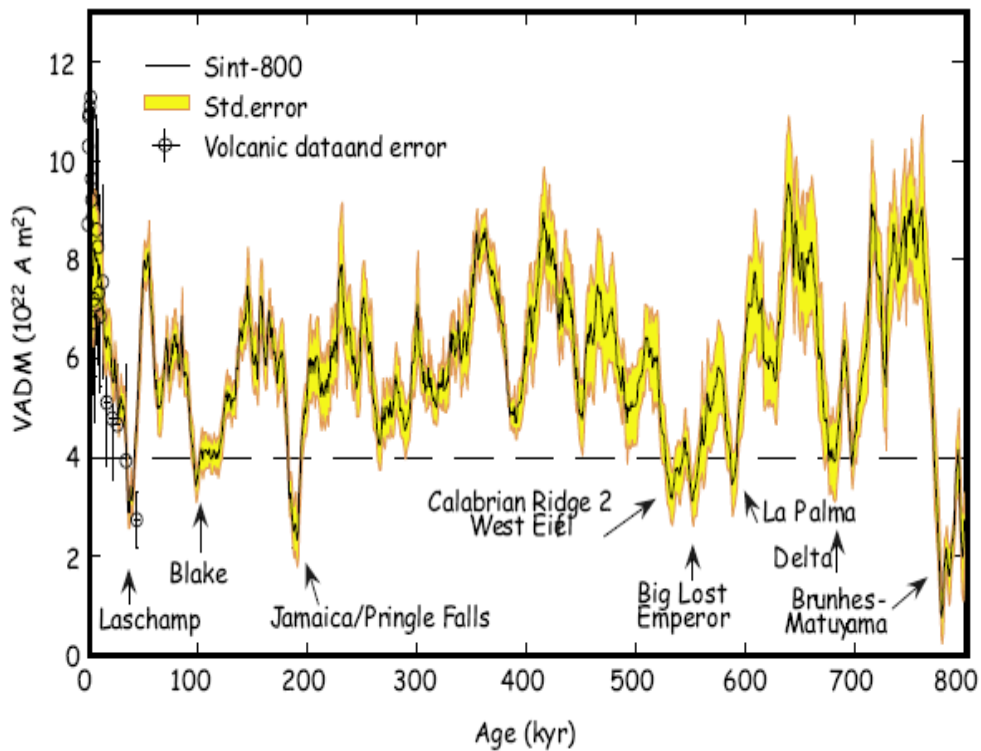　　最为著名的一条 RPI 曲线叫做 SINT800（Synthetic intensity curve since 800 ka, Guyudo and Vale, 1999, Nature）。

图 1 SINT800 RPI 曲线（Guyodo and Valet, 1999）

　　通过这条曲线，我们发现地磁场强度一直是在变化的。在~780 ka 的时候，发生了最后一次地磁极性倒转，叫做松山-布容极性倒转（Matuyama-Brunhes Boundary, MBB）。此时，强度处于非常低。之后 RPI 恢复到正常值的水平，开始了一些波动。有的时候磁场强度会低于 $4*10^{22}Am^2$，这些情形被证明都对应着地磁极性漂移事件。还有一些 RPI 低值区，到目前为止还没有明确对应着任何地磁极性事件，但是越来越多的证据表明，很可能这些 RPI 低值

区，都对应着一些小的地磁极性事件，但是受海洋沉积物分辨率的限制，无法记录。最近石笋研究有了新的进展。比如在 90 ka 左右，RPI 显示一个低值，石笋记录明确显示了一次地磁极性事件，我们称之为 post-Blake 事件。目前大家最为熟悉的地磁事件叫做 Laschamp 事件，发生在 40 ka。这个事件看似具有全球性，乃至于可以用来对海洋沉积物提供定年点。

我们把镜头拉近，看看过去 75 ka 以来的 RPI 变化特征。Laj 教授在绝对古强度和相对古强度方面做了很大的贡献。北大西洋 RPI 合成曲线目前成了 RPI 全球对比的重要标准曲线之一。显然，41 ka 的 Laschamp 事件最具有特征性。此外，在 64 ka 也有一个范围宽泛的低值区。整体来看，在 10 ka 和 75 ka 之间，有 7-8 个低值特征，这些特征常被用来进行年代框架构建。

如果沉积序列很长，记录了 MBB，那么我们很容易就获得 0.78 Ma 这个年龄控制点。但是，如果沉积物序列较短，或者沉积速率太高，都无法记录到 MBB，这时候就无法用传统的磁性地层学来构建年龄。比如，在中国东部大陆架区东海区，沉积物沉积速率太高，打个 200 米钻孔，都没发现 MBB，这对定年造成了一定的困扰。

氧同位素曲线目前是海洋沉积物中主要的定年手段之一。可是在北太平洋地区，海水上涌，其碳酸盐补偿深度（CCD）很浅，碳酸钙的虫壳被溶解了，根本无法记录有效的氧同位素曲线。

此时，RPI 曲线会提供特别重要的年龄线索。根据 RPI 和气候曲线的主要特征，同时与全球标准曲线对比，就会得到"自洽"的年龄框架。这种研究思路已经在北太平洋以及东海进行了应用，取得了很好的效果。

SINT2000 是 Jean-Pierre Valet 教授课题组的又一里程碑式的 RPI 研究成果。他们把 RPI 的变化特征拓展到过去 2 Ma。该曲线再一次证实了，在每一次地磁极性发生倒转的时候，都对应着强度的大幅度降低。从整体上来看，RPI 从 2 Ma 以来有一个逐渐上升的趋势。

我们现今的磁场整体处于一个较高的水平。过去 100 年来，地磁场的强度快速下降，让人们产生了一些恐慌感，怕强度降低后发生地磁极性倒转。对于完全的极性倒转，我们不必担心，在过去 1 Ma 以来，地磁场强度有很多次比现在更低，但是都不会引起倒转。但是，那些持续时间较短（几百-几千年）的小

事件会频发发生。对人类来说，这个时间尺度也足够对人类生存环境产生重大的影响。

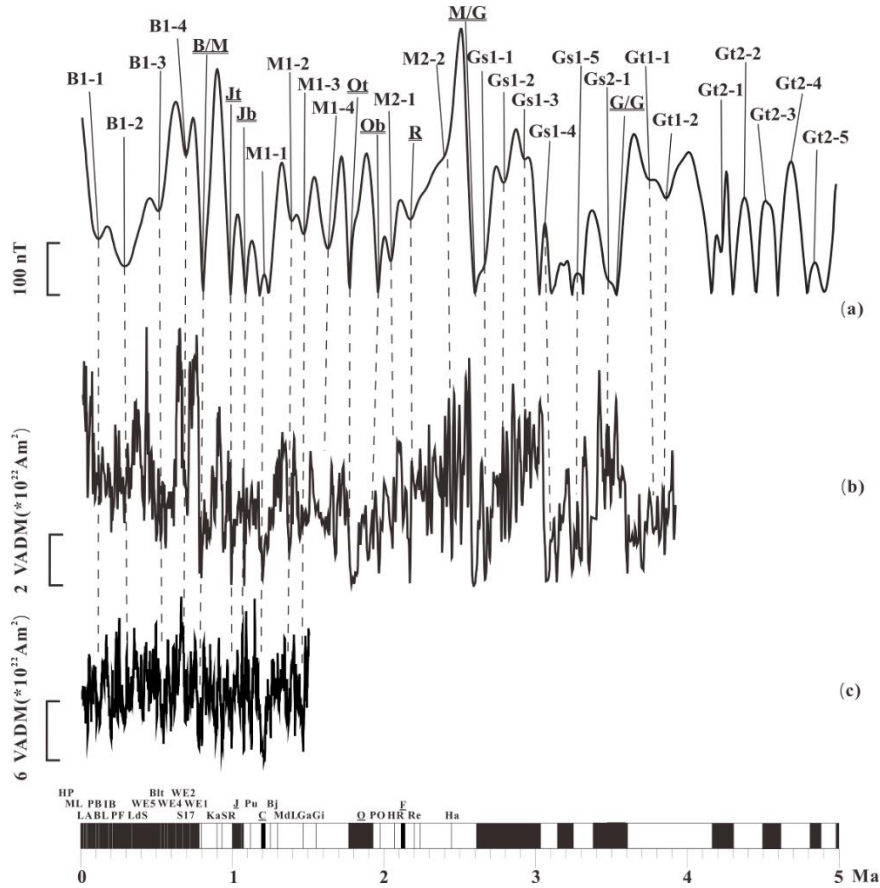随着时间尺度的延长，我们如何才能判定以上的 RPI 变化特征是合理的？在此，我们根据洋壳记录的地磁场变化特征，二者对比一下便知。

图 2 洋壳记录的地磁场强度变化（a）与海洋沉积物记录的 RPI 对比图。b）VM93 (Valet and Meynadier, 1993)，c）PISO-1500 (Channell et al.,2009).

通过对比，我们发现在低频特征上，RPI 和洋壳记录的地磁场相对变化特征几乎可以一一对比，这就说明了 RPI 记录还是能够记录地磁场信息的。但是我们也发现，在很多细节地方，还存在着差异。这有两个原因，第一，洋壳扩并不是匀速的，在扩张速率比较慢时，会丢失一些细节信息。第二，RPI 记录还受其它因素影响。但是，无论数据距离完美还有多远，就目前的曲线来看，已经揭示出地磁场强度一直在变化的特征。

文献导读

1. 西亚地区风尘通量增强与北大西洋变冷事件引发的海洋-大气偏移有关

翻译人：仲义 zhongy@sustech.edu.cn

摘要：末次冰消期以来北大西洋快速变冷事件引起全球和区域范围内的大气重组。它们对亚洲气候的影响已在季风区域进行了大量的研究，但是以西风为主的半干旱区仍然鲜为人知。作者在伊朗东南部建立了跨越 19-7 ka 之间的风尘记录，结果发现源自阿拉伯半岛和北非的沙尘羽的频繁出现与 Heinrich 1、Younger Dryas、Preboreal 振荡及 8.2 ka 的快速变冷事件导致的西风带快速南移有关。沙尘输入的升高和降低出现在这些变冷事件发生和结束的过渡时期，我们将其归因于受到北大西洋冬季海冰覆盖调节的海洋环流强度变化导致的。研究结果显示，北美冰盖的增减对西亚地区冬季气候的影响要远比欧洲冰盖的作用。

ABSTRACT: Rapid North Atlantic cooling events during the last deglaciation caused atmospheric reorganizations on global and regional scales. Their impact on Asian climate has been investigated for monsoonal domains, but remains largely unknown in westerly winddominated semiarid regions. Here we generate a dust record from southeastern Iran spanning the period 19 to 7 cal. ka B.P. We find a direct link between frequent occurrences of dust plumes originating from the Arabian Peninsula and North Africa and rapid southward shifts of the westerlies associated with changes of the winter stationary waves during Heinrich Stadial 1, the Younger Dryas, the Preboreal Oscillation, and the 8.2-ka event. Dust input rises and falls abruptly at the transitions into and out of these cooling events, which we attribute to changes in the ocean circulation strength that are modulated by the North Atlantic winter sea-ice cover. Our findings reveal that waxing and waning of North American

ice sheets have a stronger influence than those of European ice sheets on the winter climate over West Asia.
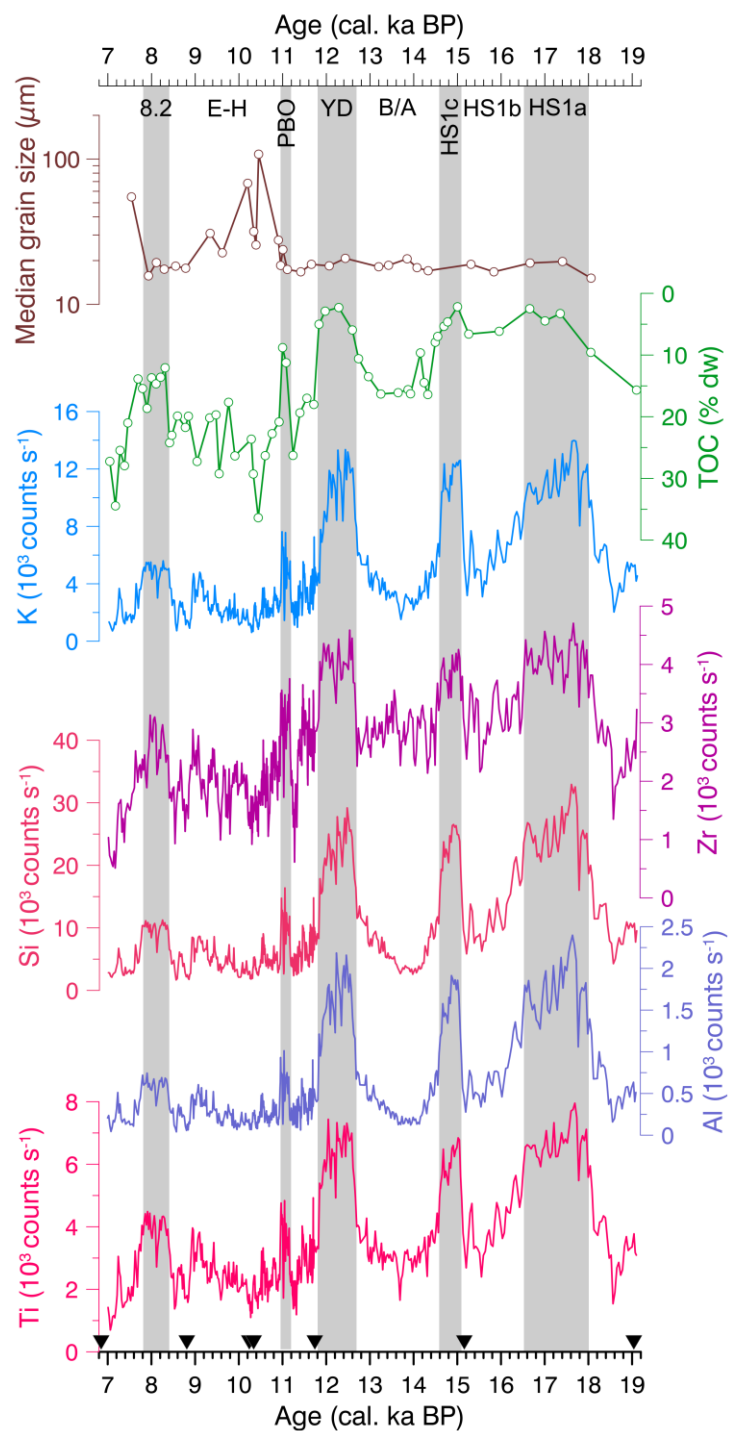

Figure 1. Downcore element abundances for immobile (Ti, Al, Si, Zr) and mobile (K) elements along with TOC (with inverted y axis) and median grain size (logarithmic scale). Gray bands mark peaks of dust input. B/A, Bølling– Allerød interstadial; E-H, Early Holocene; HS1, Heinrich Stadial 1; PBO, Preboreal oscillation; YD, Younger Dryas stadial; and 8.2, the 8.2-ka event. Black triangles at the bottom

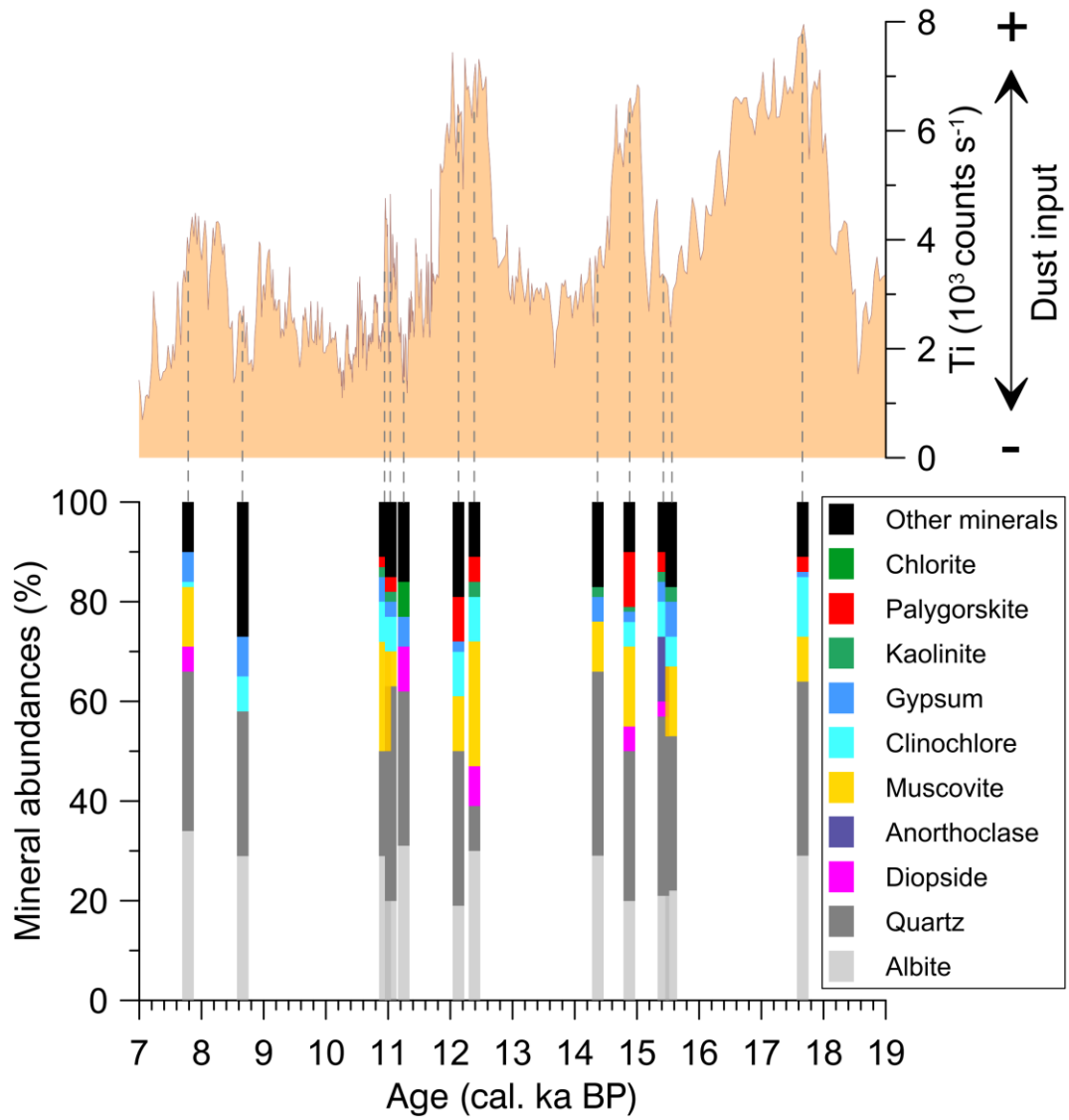indicate the position of 14C age controls for KSB.

Figure 2. Downcore variation of Ti (Top) and most abundant minerals determined by XRD analysis (Bottom).

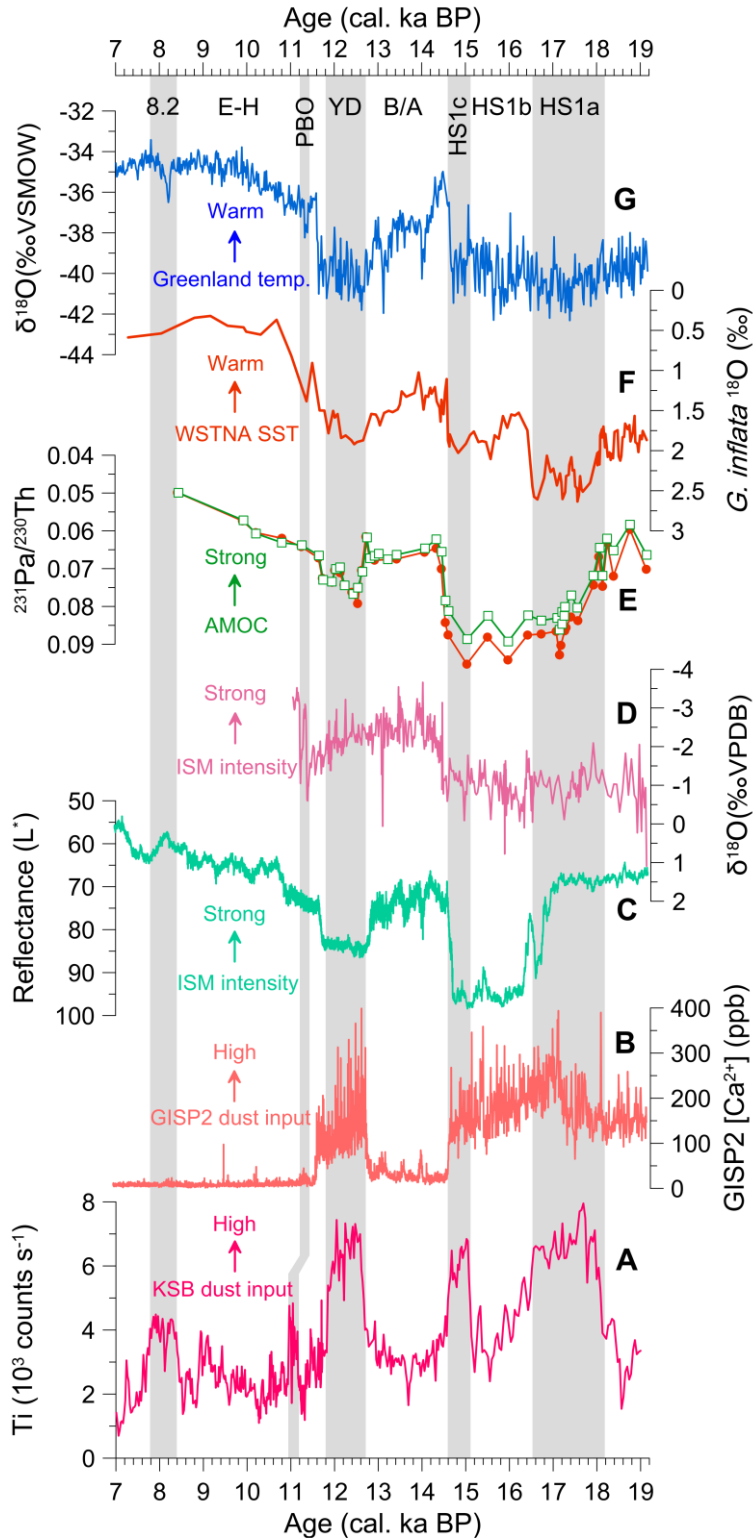Figure 3. (A, this study) Comparison of the KSB Ti record from SE Iran, representing the West Asian dust plume with paleoclimate records from Greenland ice cores, the North Atlantic Ocean and the ISM region. (B) Ca2 concentration from Greenland Ice Sheet Project (GISP) 2 ice cores (22) as aproxy for dust input in Greenland. (C) Sediment color reflectance of core SO130-289KL from the northeast

7

Arabian Sea (10) as a proxy for ISM intensity. (D) Speleothem δ18O record from Socotra, Yemen (8) as a proxy for ISM intensity. (E) 231Pa/230Th ratio from the subtropical North Atlantic (1) as a proxy for the AMOC. (F) Subtropical North Atlantic planktic foraminifera (Globorotalia inflata) δ18O from sediment core GGC5 (1) as a proxy for SST. (G) North Greenland Ice Sheet project (NGRIP) δ18O values in ‰ Vienna Standard Mean Ocean Water (SMOW) on the Greenland Ice Core Chronology 2005 (GICC05) (21) as a proxy for Greenland temperature. B/A, Bølling–Allerød interstadial; E-H, Early Holocene; HS1, Heinrich Stadial 1; PBO, Preboreal oscillation; YD, Younger Dryas stadial; and 8.2, the 8.2- ka event.

2. 古新世-始新世极热事件因化石碳氧化而延长

翻译人：蒋晓东 jiangxd@sustech.edu.cn

摘要：古新世-始新世极热事件（PETM）期间大量碳的快速释放引起全球碳同位素负漂移。碳同位素负漂移的延迟恢复表明二氧化碳的持续输入。但对于二次输入碳的来源还并无一致的结论。本研究表明二次输入的碳很可能部分来自沉积化石碳的氧化。作者测定了美国中大西洋陆架海岸热演化生物标志物，构建了生物标志物混合模型来限定美国中大西洋陆架和坦桑尼亚海岸化石碳的量，以此估算化石碳的堆积速率确定了来自化石碳的全球二氧化碳释放量。本研究提供了事件开始后 10-20 kyr 关于化石碳释放入海洋中的数量级，二氧化碳的释放量在 10^2 到 10^4 PgC 之间。该估算量能够持续的维持大气二氧化碳量在较高的水平，而延长碳同位素负漂移。即使考虑到沉积速率的不确定性，这些结果仍能指示古老沉积物中碳的侵蚀、迁移和氧化的进一步强化，对延迟气候系统的恢复可达到数千年。

ABSTRACT: A hallmark of the rapid and massive release of carbon during the Palaeocene－Eocene Thermal Maximum is the global negative carbon isotope excursion. The delayed recovery of the carbon isotope excursion, however, indicates that CO_2 inputs continued well after the initial rapid onset, although there is no consensus about the source of this secondary carbon. Here we suggest this secondary input might have derived partly from the oxidation of remobilized sedimentary fossil carbon. We measured the biomarker indicators of thermal maturation in shelf records from the US Mid-Atlantic coast, constructed biomarker mixing models to constrain the amount of fossil carbon in US Mid-Atlantic and Tanzania coastal records, estimated the fossil carbon accumulation rate in coastal sediments and determined the range of global CO_2 release from fossil carbon reservoirs. This work provides evidence for an order of magnitude increase in fossil carbon delivery to the oceans that began ~10－20 kyr after the event onset and demonstrates that the oxidation of remobilized fossil carbon released between 10^2 and 10^4 PgC as CO_2 during the body of the Palaeocene－Eocene Thermal Maximum. The estimated mass is sufficient to have sustained

the elevated atmospheric CO_2 levels required by the prolonged global carbon isotope excursion. Even after considering uncertainties in the sedimentation rates, these results indicate that the enhanced erosion, mobilization and oxidation of ancient sedimentary carbon contributed to the delayed recovery of the climate system for many thousands of years.
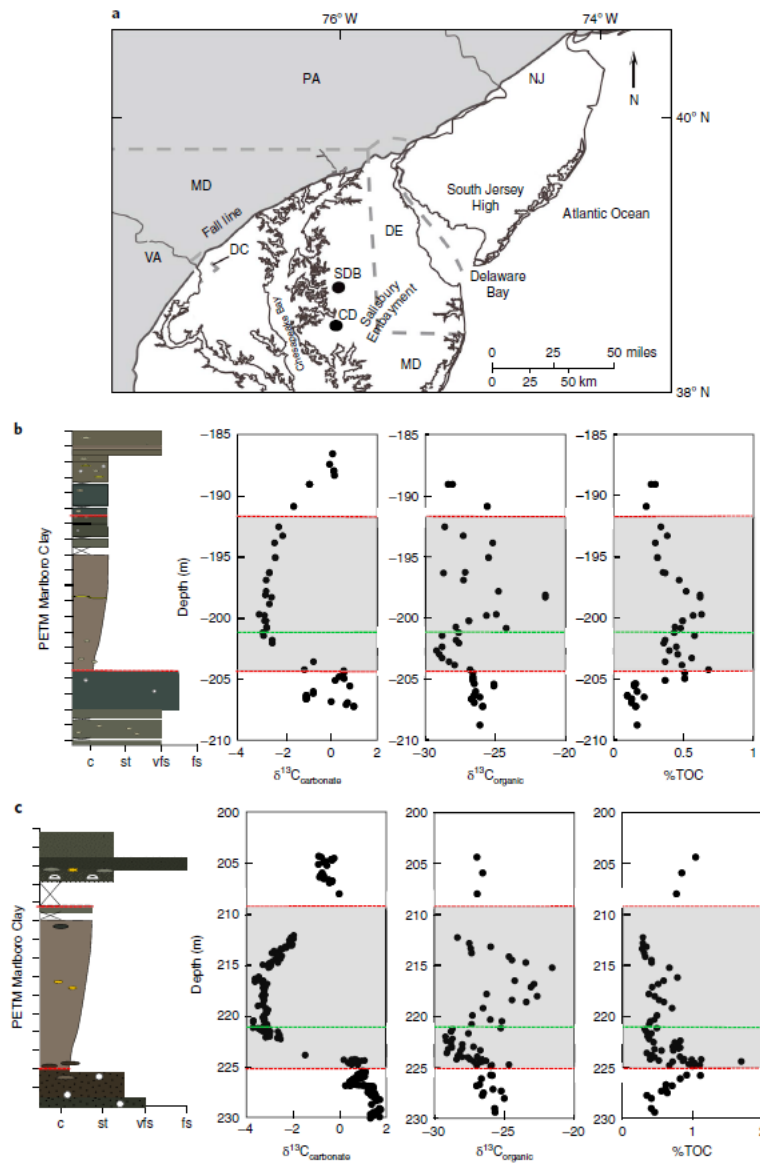

Figure 1. Percent organic carbon and carbonate and organic isotope records plotted against depth at SDB and CamDor inner shelf sites. **a**, Location of SDB and CamDor (CD) cores. The Upper Palaeocene Aquia formation is overlain by 13.8 m (CamDor) and 14.9 m (SDB) of Lower Eocene Marlboro Clay, above which is a contact with the Eocene Nanjemoy Formation. **b**, **c**, %TOC, carbonate and organic CIEs are presented for the inner-shelf Palaeo‑Potomac transect records of SDB (b) and CamDor (c). The grey

10

shaded areas represent the PETM Marlboro Clay, bounded by red dotted lines. The start of the positive

δ $^{13}C_{org}$ enrichment is marked by a green dotted line. Lithology is designated as: **c**, clay; st, silt; vfs, very
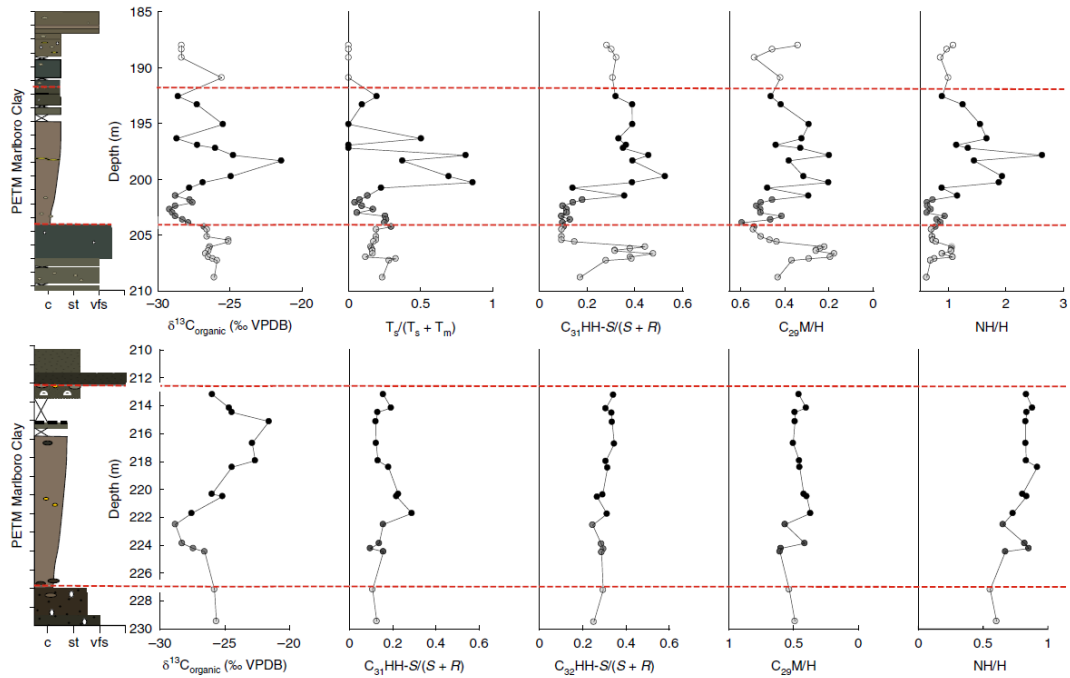
fine sand; fs, fine sand.

Figure 2. Biomarker thermal maturity ratios at SDB (top) and CamDor (bottom) demonstrate a source

change during the PETM body. Thermal maturity ratios are plotted alongside the organic isotope record

and shaded by timing during the PETM (light grey, pre-PETM; dark grey, PETM onset; black, PETM

body at $\delta^{13}C_{org}$ enrichment onset; white, post-PETM). $T_s/(T_s + T_m)$, C_{31}-homohopane $(C_{31}HH)$-$S/(S + R)$,

C_{32}-homohopane $(C_{32}HH)$-$S/(S + R)$ and norhopane/hopane (NH/H) increase with thermal maturity; C_{29}-

moretane/(moretane + hopane) (C29M/H) decreases with thermal maturity. The PETM interval is

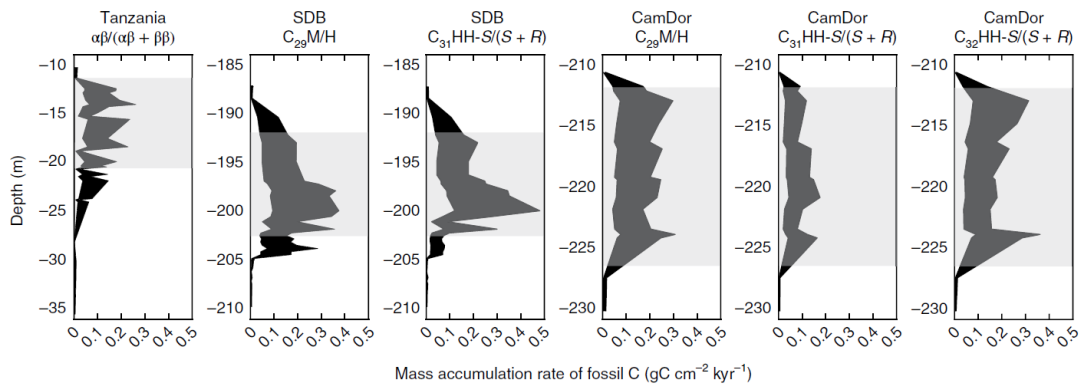bounded by red dotted lines. VPDB, Vienna Pee Dee Belemnite.

Figure 3. Percent organic carbon and carbonate and MARs of fossil C show an increase in fossil C delivery to sediments during the PETM body. MARs are based on fossil C mixing models during the PETM body from Tanzania ($\alpha\beta$ /($\alpha\beta$ + $\beta\beta$) hopanoid isomerization), SDB (C_{29}-M/M + H, C_{31}-HH-*S/S* + *R*), CamDor (C_{29}-M/M + H, C_{31}-HH-*S/S* + *R*, C_{32}- HH-*S/S* + *R*) and the uncertainty around linear sedimentation rates. The *x* axis represents the MARs of fossil C, and the *y* axis represents the depth in each section. Leftward bounds on each plot mark the lower-end MAR estimate and rightward bounds mark the upper MAR estimate based on 0.5–2 times the measured sedimentation rate. The grey shaded areas indicate the PETM interval. Data from all the records show an elevated MAR during the PETM body relative to the background delivery of fossil C.

3. 南非布什维尔德杂岩体中的 Rustenburg 层状岩套的快速冷却：来自黑云母 $^{40}Ar/^{39}Ar$ 地质年代学的约束

翻译人：冯婉仪 fengwy@sustech.edu.cn

摘要: 尽管层状镁铁质侵入岩的冷却历史对了解岩浆房过程和具有经济价值的贵金属矿床的形成至关重要，但由于地质年代学的限制，这仍然是一个谜。我们对南非布什维尔德杂岩体中的 Rustenburg 层状岩套（RLS）中的黑云母开展了系统的 $^{40}Ar/^{39}Ar$ 地质年代学研究。来自 10 个样品（这些样品涵盖了~5.5 km 的 RLS 岩层）的黑云母颗粒分析结果得到的加权平均坪年龄范围为 2056.3 ± 3.2 Ma 至 2052.0 ± 7.6 Ma（2σ），所有年龄都在 2 个 σ 范围内（σ-95%置信水平）重叠。所有的黑云母坪年龄的加权平均值为 2054.47 ± 0.84 Ma（2σ，n = 30，加权偏差的均方 = 0.23，P = 1.00；当考虑所有外部不确定性时，误差增加到 ± 21 Ma）。本文得到的黑云母 $^{40}Ar/^{39}Ar$ 年龄与已发表的 U-Pb 锆石年龄的重叠表明，RLS 迅速冷却到黑云母的封闭温度，整个岩层的冷却速率约为 1000 ℃ m.y.$^{-1}$。由于热液系统与 RLS 的侵位相关，热建模需要增加热损失来产生推测的快速冷却速率。先前报道的 UG-2 和 MG-1 铬铁矿矿层以及 Merensky Reef 的年轻的黑云母 $^{40}Ar/^{39}Ar$ 年龄很可能是热液流体局部晚期循环的产物。在剩余的岩层中没有类似的年轻的黑云母 $^{40}Ar/^{39}Ar$ 年龄，这表明晚期热液事件可能局限于铬铁矿矿层和 Merensky Reef 中。

ABSTRACT: Despite their importance to understanding magma chamber processes and the formation of economically viable precious metal deposits, the cooling histories of layered mafic intrusions remain enigmatic due to limited geochronologic constraints. We provide a comprehensive $^{40}Ar/^{39}Ar$ study of biotite throughout the Rustenburg Layered Suite (RLS) of the Bushveld Complex, South Africa. Analyses of individual biotite grains from 10 samples, encompassing ~ 5.5 km of RLS

stratigraphy, yielded weighted mean plateau ages that all overlap at 2σ (α-95% confidence level) and range from 2056.3 ± 3.2 Ma to 2052.0 ± 7.6 Ma (2σ). A weighted mean of all biotite plateau ages yielded an age of 2054.47 ± 0.84 Ma (2σ, n = 30, mean square of weighted deviates = 0.23, P = 1.00; ± 21 Ma fully propagated). The overlap between our ^{40}Ar/^{39}Ar biotite and published U-Pb zircon ages suggests that the RLS cooled rapidly to the closure temperature of biotite, with cooling rates on the order of 1000 °C m.y.$^{-1}$ throughout the stratigraphy. Thermal modeling requires enhanced heat loss, due to the hydrothermal system associated with the emplacement of the RLS, to produce the inferred rapid cooling rates. Previously reported young ^{40}Ar/^{39}Ar biotite ages from the UG-2 and MG-1 chromitite seams and the Merensky Reef are likely a product of localized late-stage circulation of hydrothermal fluids. The lack of similarly young ^{40}Ar/^{39}Ar biotite ages from the remainder of the stratigraphy suggests that late-stage hydrothermal events were potentially localized to chromitites and the Merensky Reef.
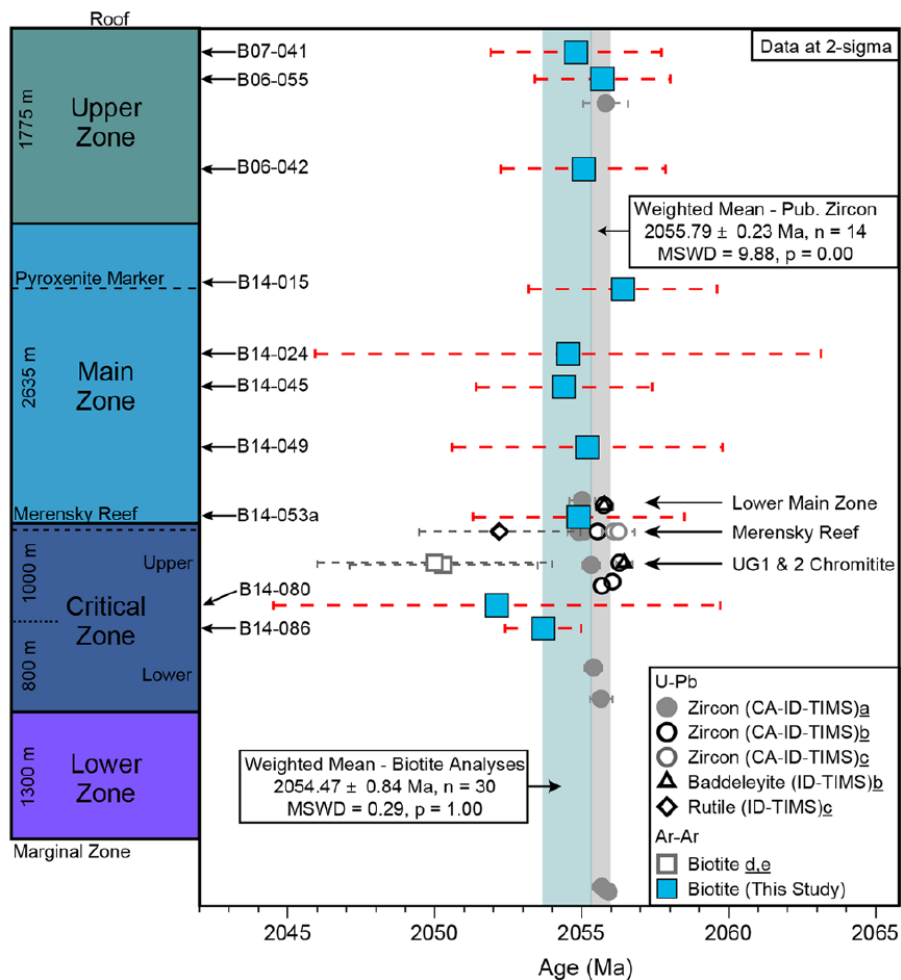

Figure 1. Available high-precision chronology (2σ uncertainties, internal errors) against generalized

stratigraphic column of the Eastern Limb of the Rustenburg Layered Suite (RLS), Bushveld Complex, South Africa. [40]Ar/[39]Ar biotite ages are weighted mean plateau ages (this study; filled blue squares) of multiple analyses from a single sample. Weighted mean of all 40Ar/39Ar biotite plateau ages from this study is indicated by the blue shaded region. Published U-Pb zircon ages are: a—Zeh et al. (2015), b—Mungall et al. (2016), and c—Scoates and Wall (2015). Weighted mean of U-Pb zircon ages from listed studies is denoted by vertical gray region. Published 40Ar/39Ar biotite ages are: d and e—Cassata et al. (2009) and Nomade et al. (2004). References for published U-Pb ages of baddeleyite and rutile are denoted by b and c, respectively. MSWD—mean square of weighted deviates; CA-ID-TIMS—chemical abrasion–isotope dilution–thermal ionization mass spectrometry.
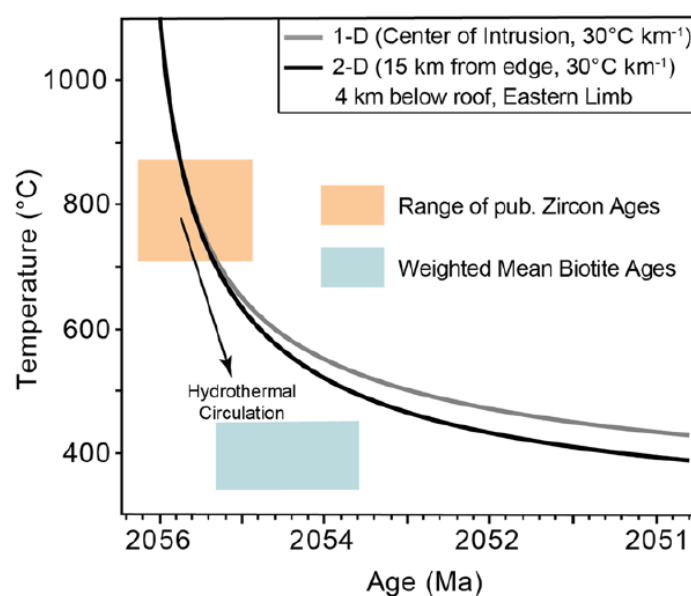

Figure 2. Conductive cooling models solving for 4 km below the top of the 8-km-thick Rustenburg Layered Suite (RLS), Bushveld Complex, South Africa, assuming 30 °C km^{-1} geotherm (Gibson and Wallmach, 1995) and 4 km roof. For gray curve (1-D), heat is lost through the top and bottom of the RLS. For black curve (2-D), heat is also lost through the sides of the RLS (solved for rocks 15 km from contact with host rock). The range of published mean U-Pb zircon ages and their measured Ti-in-zircon temperatures are indicated by the orange shaded area. Weighted mean ages of biotite [40]Ar/[39]Ar plateau ages (this study) and their assumed closure temperature (Tc) are represented by the blue shaded region (internal errors).

4. 国际大洋发现计划 355 航次修订阿拉伯海东部 Laxmi 海盆的年代地层框架

翻译人：李园洁 liyj3@sustech.edu.cn

摘要：国际大洋发现计划 355 航次在阿拉伯海东部 Laxmi 海盆打钻的 U1456 和 U1457 记录了南亚季风对喜马拉雅山的风化和侵蚀的影响。本文结合了生物地层学，磁性地层学和锶同位素地层学，修订这两个钻孔的年代地层学框架。这两个钻孔的沉积物剖面相似，我们依据不整合面或块体搬运沉积(MTD)将其分为六个单元。单元 1 位于 MTD 之下，在 U1456 孔处于中新世早期-中期，在 U1457 孔处于古新世早期。中新世末期 (约 9.83–9.69 Ma) MTD (单元 2) 的侵入形成的不整合面 (U1) 将单元 1 和单元 2 分开，通过岩性的显著变化来识别。单元 3 由中新世晚期渐变砂岩夹层的近海沉积物组成，与单元 4 由一个 0.5-0.9 Myr 的不整合面 (U2) 隔开。单元 4 由上中新世夹层泥岩和砂岩以及近海沉积白垩组成，在大约 8-6 Ma 期间沉积。单元 4 和单元 5 由一个包含中新世-上新世边界的 1.4-1.6 Myr 的沉积间断 (U3) 隔开。单元 5 由上新世-下更新世硅质碎屑沉积物组成，与单元 6 由下更新世沉积物中 0.45 Myr 的沉积间断 (U4) 隔开。单元 6 包括一堆厚的快速沉积的更新世砂岩和泥土，上覆自约 1.2 Ma 沉积的近海沉积物。

ABSTRACT：International Ocean Discovery Program Expedition 355 drilled Sites U1456 and U1457 in Laxmi Basin (eastern Arabian Sea) to document the impact of the South Asian monsoon on weathering and erosion of the Himalaya. We revised the chronostratigraphic framework for these sites using a combination of biostratigraphy, magnetostratigraphy and strontium isotope stratigraphy. The sedimentary section at the two sites is similar and we divided it into six units bounded by unconformities or emplaced as a mass-transport deposit (MTD). Unit 1 underlies the MTD, and is of early-middle Miocene age at Site U1456 and early Paleocene age at Site U1457. An unconformity (U1) created by emplacement of the MTD (unit 2) during the late Miocene Epoch (at c. 9.83–9.69 Ma) separates units 1 and 2 and is identified by a marked change in lithology. Unit 3 consists of

hemipelagic sediment with thin interbeds of graded sandstone of late Miocene age, separated from unit 4 by a second unconformity (U2) of 0.5-0.9 Myr duration. Unit 4 consists of upper Miocene interbedded mudstone and sandstone and hemipelagic chalk deposited between c. 8 and 6 Ma. A c. 1.4-1.6 Myr hiatus (U3) encompasses the Miocene-Pliocene boundary and separates unit 4 from unit 5. Unit 5 includes upper Pliocene-lower Pleistocene siliciclastic sediment that is separated from unit 6 by a c. 0.45 Myr hiatus (U4) in the lower Pleistocene sediments. Unit 6 includes a thick package of rapidly deposited Pleistocene sand and mud overlain by predominantly hemipelagic sediment deposited since c. 1.2 Ma.
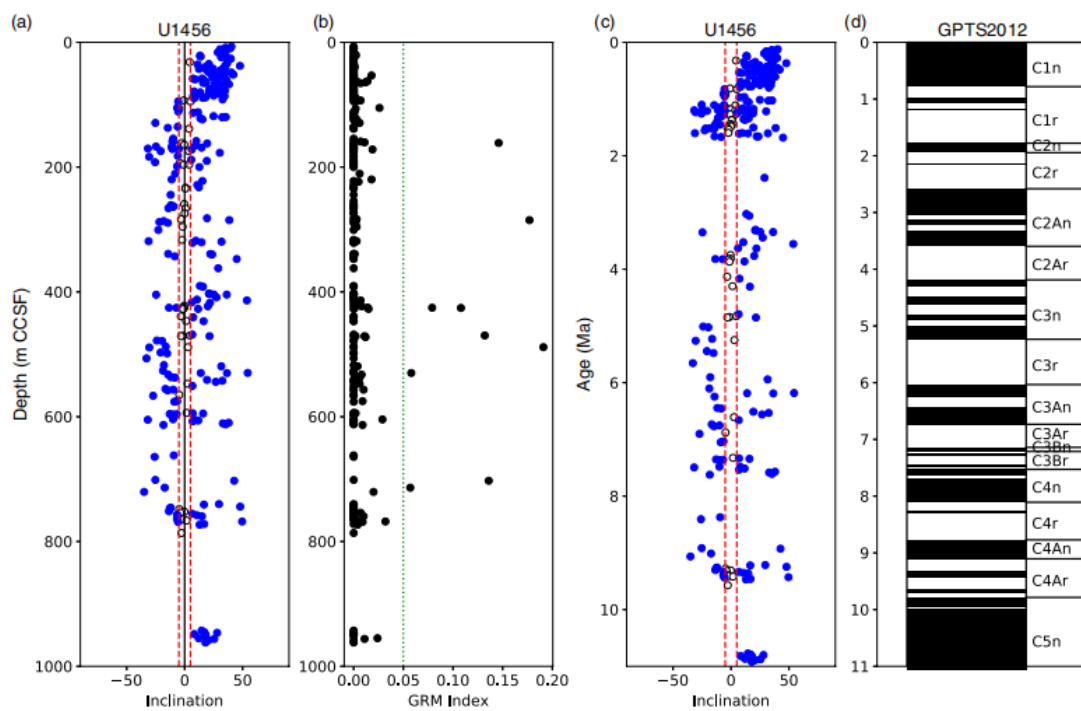

Figure 1. Revised magnetostratigraphic data and interpretations for Site U1456. (a) Inclinations versus composite depth (m CCSF). (b) Gyromagnetic resonance (GRM) index as described in the text. (c) As for (a), but plotted against inferred age. (d) Geomagnetic polarity time scale of Gradstein et al. (2012).
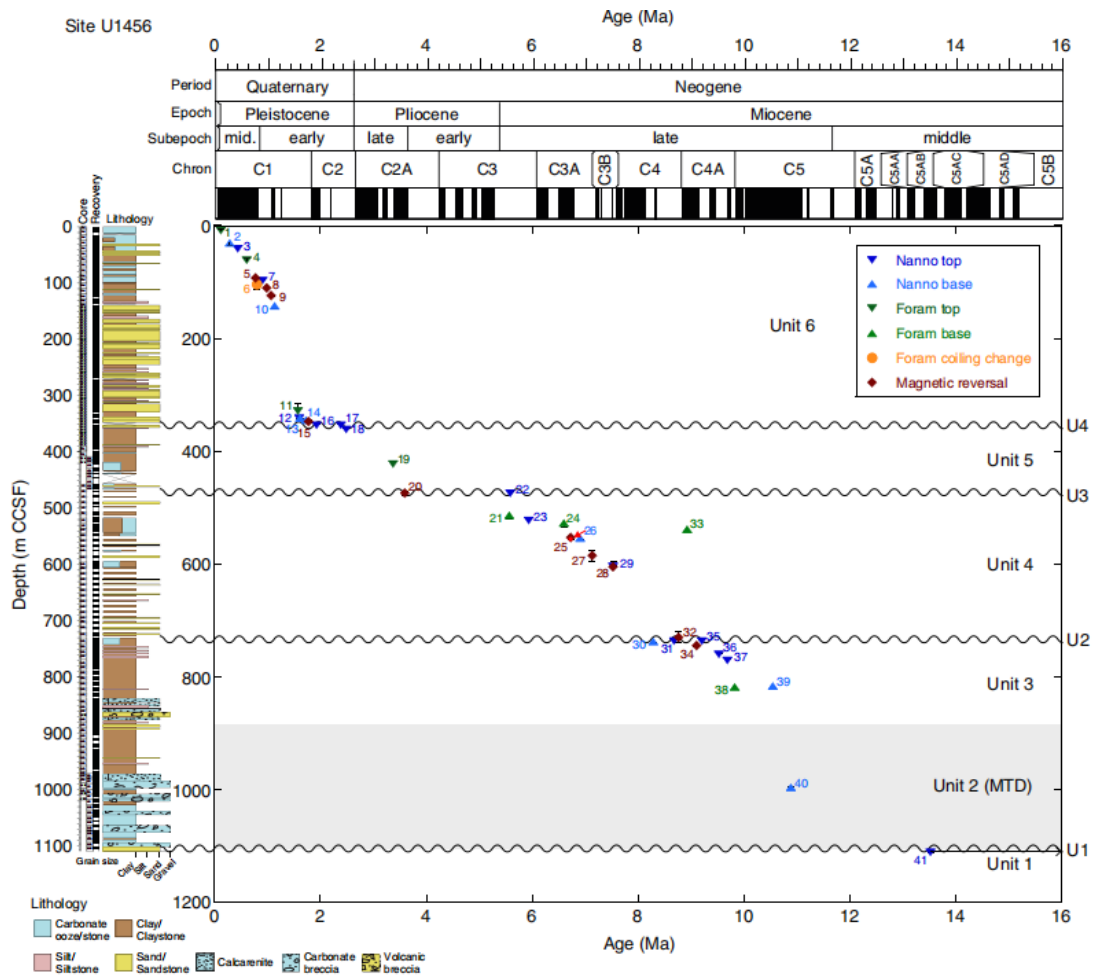
Figure 2. Chronostratigraphic framework for Site U1456. Blue triangles are calcareous nannofossil events (up are tops, down are bases); green triangles are foraminifera events (up are tops, down are bases); orange circle is change in foraminifer coiling direction; and maroon diamonds are palaeomagnetic chron boundaries. Black lines represent error bars (both age and depth). See text (Section 5.d) for discussion of red arrow. Number represents chronostratigraphic event (refer to datum labels in Table 1).

5. 对墨西哥中部历史火山岩的多种古强度方法研究：寻找准确的古强度测定

翻译人：柳加波 liujb@sustech.edu.cn

摘要：本文对 2ka 左右的 Xitle 火山岩（墨西哥南部盆地）进行了系统的岩石磁学和古强度研究，以评估新鲜、广泛裸露的熔岩流记录的古地磁信息的可靠性。我们对来自六个熔岩流的古地磁样品采用了多种方法进行古地磁研究：Thellier-Coe、IZZI 和多样本方法。从 4-6 号熔岩流的样品中，通过 Thellier-Coe、IZZI 和 Thellier-Coe 校正的 IZZI 方法获得平均古强度分别为 68.4 µT（$\sigma = \pm 5.6$ µT）、63.9 µT（$\sigma = \pm 5.8$ µT)和 61.5 µT（$\sigma = \pm 4.3$ µT）。对于同样的火山岩样品，尽管多样本方法获得古强度通常要比其他方法要低，但是多样本方法获得的 5 号熔岩流的古强度为 61.8 µT，这和 Thellier 方法获得古强度非常接近。基于获得的古地磁结果，3-6 号熔岩流和 Xitle 火山喷发有关，而 1-2 号熔岩流的年代更老。不同熔岩流的考古磁学定年，以及二十年前提出的 Xilte 火山具有多次喷发年代，也验证了我们的推断。采用更严格的检验标准，并考虑冷却速率校正，能够再稍微减少结果的不确定性。在这项研究中采用的多种古强度方法，再加上系统的岩石磁学实验，可能会最终提高古强度测定的准确性。

ABSTRACT: An inclusive rock-magnetic and absolute paleointensity survey of the ~2-ka-old Xitle volcano (southerly Basin of Mexico) was undertaken to assess the faithfulness of the paleomagnetic log carried by fresh, widely exposed and well-preserved lava flows. Paleomagnetic samples from six lava flows were subjected to paleointensity analysis with a multi-method approach: the Thellier–Coe, IZZI, and multi-specimen methods. Overall mean flow PI values from flows 4–6 obtained by the Thellier-type methods used yielded 68.4 µT ($\sigma = \pm 5.6$ µT), 63.9 µT ($\sigma = \pm 5.8$ µT) and 61.5 µT ($\sigma = \pm 4.3$ µT) for the TC, IZZI, and IZZI with CR correction methods, respectively. Although multi-specimen paleointensity results were, in general, lower than that obtained with the other methods for the same flows, that for Flow 5 (61.8 µT) was very similar to those obtained with

the Thellier-type methods. Based on the results obtained, this lava flows sequence could correspond to two eruptive periods; one related with the Xitle volcano (flows 3–6), and another older (flows 1 and 2). The combined archeomagnetic dating of the different flows reinforces this hypothesis, as well as the multi-modal distribution for the age of the Xitle, proposed two decades ago. The application of stricter acceptance criteria and consideration of cooling-rate correction could slightly reduce the scattered observations. The multi-method approach employed under this study, combined with detailed rock-magnetic experiments, may definitively increase the accuracy of paleointensity determinations.
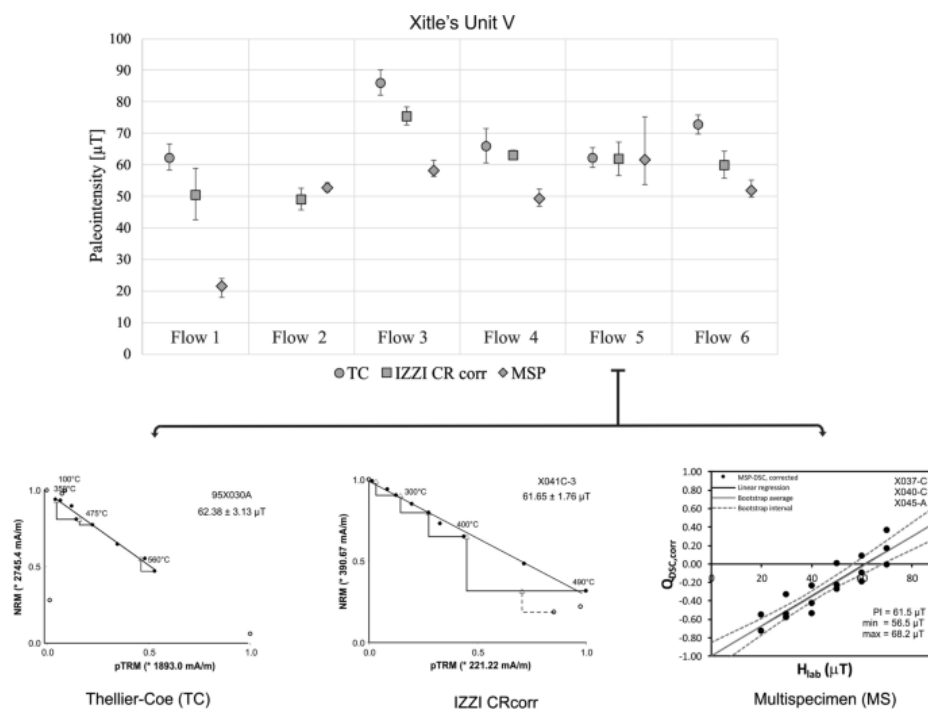

Fig 1: Up: Comparison of PI results obtained by the different methodologies used (TC, IZZI CRcorr, and MS) for the 6 flows analyzed. Error bars represent the corresponding standard deviations in the case of TC and IZZI CRcorr results, while for the MS data to the Min and Max values obtained. Below: Representative Arai plot (Nagata et al. 1965b) obtained from the TC experiments; Representative Arai plot (Nagata et al. 1965b) obtained from the IZZI CRcorr experiments; Representative plot obtained from the MS experiments.

6. 一条晚始新世-渐新世流经长江上游与南海之间的河流

翻译人：刘伟 inewwway@163.com

摘要：我们对古近纪是否存在一条主要流经青藏高原东南部和长江上游而注入南海的河流的模型进行了检验。其中主要是通过对越南北部和中国西南地区古近系沉积岩中的锆石 U−Pb 年龄来对该模型进行验证。我们应用了一系列的统计检验来比较岩石的 U-Pb 年龄谱，以突出它们之间的差异和相似性以及确定潜在的源区。蒙特卡洛混合模型表明，侵蚀主要来自印支地块和松潘甘孜地块，扬子克拉通地块则较少。部分锆石指示了局部侵蚀和沉积的特征，其他锆石则与越南北部地区和中国始新世的剑川盆地、古新世-渐新世的思茅盆地、渐新世-中新世的元江盆地表现出较广泛的相似性。西藏昌都地块较年轻(200 Ma)锆石的存在，不太能通过较老沉积岩的侵蚀再循环来解释，这就暗示了在晚始新世-渐新世存在连接西藏东南和南海的区域性水系。南海近海的碎屑锆石表现出初步的局部侵蚀特征，但在晚渐新世表现为与延伸至西藏东南的一条河流有联系。元江盆地早中新世区域物源向局部物源的转变，表明了区域高原隆升作用下古水系被破坏的时间。

ABSTRACT: We test the hypothesis of a major Paleogene river draining the SE Tibetan Plateau and the central modern Yangtze Basin that then flowed south to the South China Sea. We test this model using U-Pb dated detrital zircon grains preserved in Paleogene sedimentary rocks in northern Vietnam and SW China. We applied a series of statistical tests to compare the U-Pb age spectra of the rocks in order to highlight differences and similarities between them and with potential source bedrocks. Monte Carlo mixing models imply that erosion was dominantly derived from the Indochina and Songpan-Garzê Blocks and to a lesser extent the Yangtze Craton. Some of the zircon populations indicate local erosion and sedimentation, but others show close similarity both within northern Vietnam, as well as more widely in the Eocene Jianchuan, Paleocene-Oligocene Simao, and Oligocene-Miocene Yuanjiang basins of China. The presence of younger (<200 Ma) zircons from the Qamdo Block of Tibet is less easily explicable in terms of recycling by erosion of older

sedimentary rocks and implies a regional drainage linking SE Tibet and the South China Sea in the Late Eocene-Oligocene. Detrital zircons from offshore in the South China Sea showed initial local erosion, but with a connection to a river stretching to SE Tibet in the Late Oligocene. A change from regional to local sources in the Early Miocene in the Yuanjiang Basin indicates the timing of disruption of the old drainage driven by regional plateau uplift.
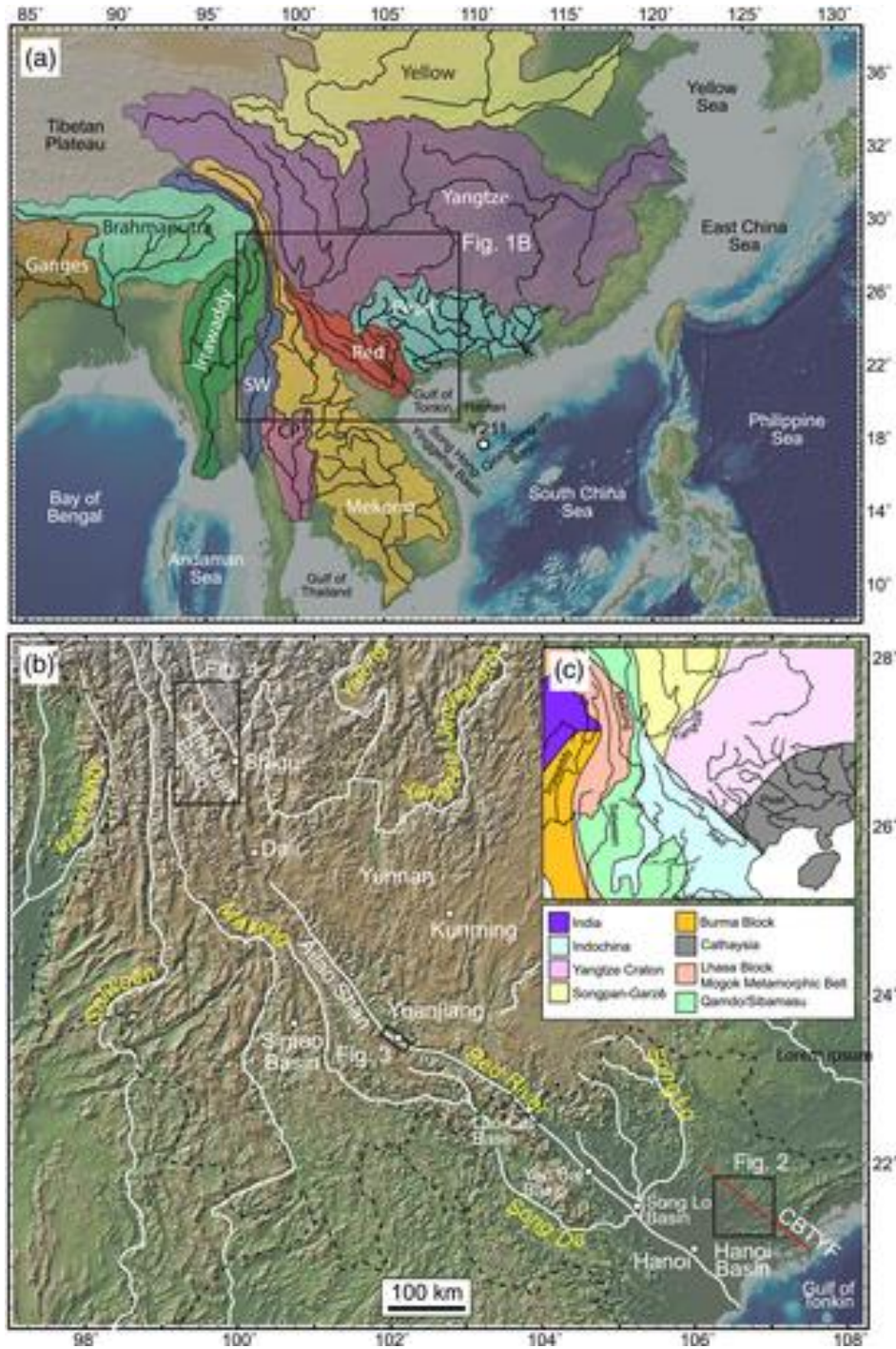

Figure 1. (a) Shaded topographic map of East and SE Asia showing the major modern river basins and the location of Well Y211 (Lei et al., 2019); CP = Chao Phraya; SW = Salween. (b) Shaded topographic

map of the study region showing the major river systems and geographic regions mentioned in the text. CBTYF = Cao Bang-Tien Yen Fault Zone. International borders shown as dashed black line. River names are show in yellow italic text. (c) Simplified tectonic map of the region showing the major tectonic blocks and the course of the major rivers discussed in this work, modified from original map of Searle et al. (2017).
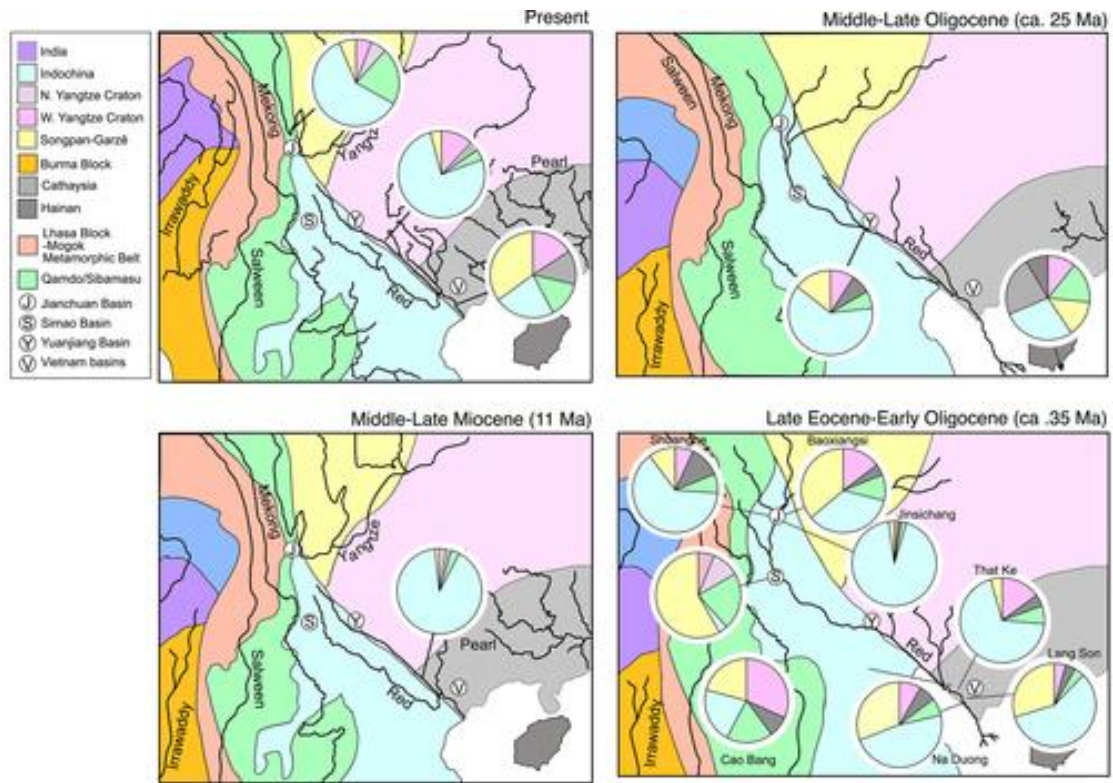

Figure 2. Evolving paleogeography of SE Tibetan Plateau and northern Indochina showing the proposed development of major river systems since the Late Eocene. Pie diagrams show the proposed breakdown of the zircon population based on source and the unmixing calculations discussed in the text for each sample at the time of their deposition.

7. 青藏高原湖泊对环境变化的响应：趋势、模式和机制

翻译人：曹伟 11930854@QQ.com

摘要：青藏高原是世界上海拔最高、面积最大的高原，其分布广泛的天然湖泊由于全球气候变暖而受到大量关注。在这篇文章中，我们研究了青藏高原上的湖泊演变、空间格局和驱动机制。从1976年至90年代中期，湖区面积、水位和水量的变化呈现出轻微的下降趋势，之后又呈现出持续的快速上升趋势。空间格局显示，高原内北部湖泊整体增长而南部湖泊减少，同期北部大部分湖泊变冷而南部湖泊变暖，而且北部的冰盖持续时间比南部更长。湖泊温度的变化与水位变化和湖泊冰期呈负相关。降水增加是湖泊蓄水量增加的主要原因，其次是冰川与冻土的融化。自90年代中期以来的十年或更长时间的湖泊扩张可能是由于大西洋年代际震荡的正相位所驱动的，而1997/1998和2015/2016年明确的湖泊面积/水位拐点则归因于强厄尔尼诺事件。近期内，湖泊将会继续扩张。未来迫切需要跨学科的湖泊研究，以提高对气候-冰冻圈-水圈相互作用和水资源管理的认识。

ABSTRACT: The wide distribution of natural lakes over the Tibetan Plateau, the highest and largest plateau on Earth, have received extensive attention due to global warming. In this Review, we examine lake evolution, spatial patterns and driving mechanisms over the Tibetan Plateau. The changes in lake area, level and volume show a slight decrease from 1976 to the mid-1990s, followed by a continuous rapid increase. The spatial patterns show an overall lake growth in the north of the inner plateau against a reduction in the south, which are accompanied by most of the lakes cooling in the north against warming in the south, and longer ice cover duration in the north compared with the south. The changes in lake temperature are negatively correlated with water level variations and lake ice duration. Enhanced precipitation is the dominant contributor to increased lake water storage, followed by glacier mass loss and permafrost thawing. The decadal or longer lake expansion since the mid-1990s could have been driven by the positive phase of Atlantic Multidecadal Oscillation, and clear inflection points of lake area/level identified in 1997/1998 and 2015/2016 are attributed

to strong El Niño events. In the near-term, the lakes will continue to expand. Future interdisciplinary lake studies are urgently required to improve understanding of climate-cryosphere-hydrosphere interactions and water resources management.
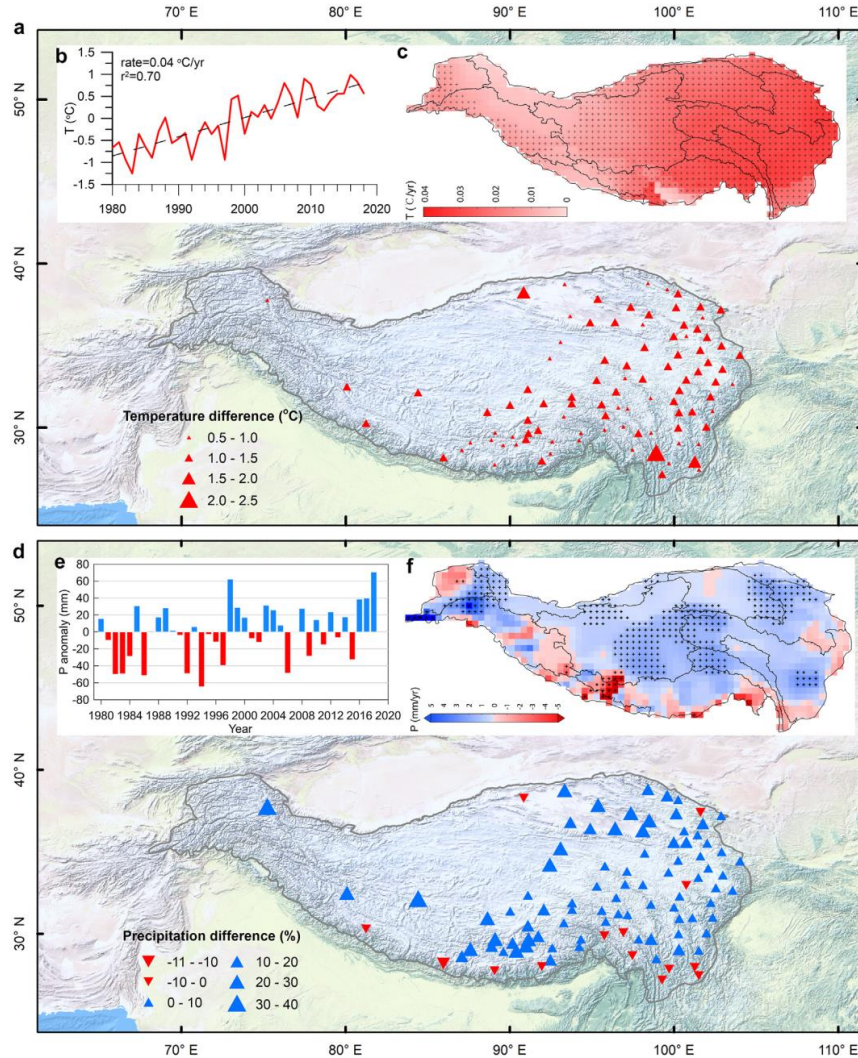

Figure 1. Temperature (T) and precipitation (P) changes. a) T difference between 1998−2018 and 1980−1997 from China Meteorological Administration (CMA) weather station data. b) Annual T anomalies between 1980 and 2018 for the TP. c) Change in T derived from the CRU T data for 1970−2016. d) P difference between 1998−2018 and 1980−1997 from CMA weather station data. e) Anomaly of annual P averaged over all stations for 1980−2018. f) Change in P derived from GPCC data for 1970−2016. The "+" indicates pixels with significant linear trends at a 95% confidence level.

8. 末次冰期冰盖地形对东亚夏季风的动态影响

翻译人：杨会会 11849590@mail.sustech.edu.cn

摘要：末次冰期期间冰盖地形对东亚夏季风的影响，在模型配置的层次结构中使用模型 CCSM3 进行了研究。研究发现，冰盖的退缩导致了东亚夏季风强度减弱，其中冰盖厚度的减少起着主要作用。冰盖厚度降低通过改变中纬度急流的位置，以及改变北半球静止波，来削弱东亚夏季风强度。在急流移动机制中，冰盖的降低使西风急流北移，夏季亚热带上空的西风急流减少，这减少了 EASM 区上空的干热平流，进而减少了该区的降水。在静止波机制中，冰盖的降低导致了沿西风波向 EASM 区传播的异常静止波列，产生等效正压低响应，这导致低对流层南风（southerlies）减少，进而减少了进入东亚的干热平流，从而导致 EASM 降水减少。

ABSTRACT: The effect of ice sheet topography on the East Asian summer monsoon (EASM) during the Last Glacial Maximum is studied using CCSM3 in a hierarchy of model configurations. It is found that receding ice sheets result in a weakened EASM, with the reduced ice sheet thickness playing a major role. The lower ice sheet topography weakens the EASM through shifting the position of the midlatitude jet, and through altering Northern Hemisphere stationary waves. In the jet shifting mechanism, the lowering of ice sheets shifts the westerly jet northward and decreases the westerly jet over the subtropics in summer, which reduces the advection of dry enthalpy and in turn precipitation over the EASM region. In the stationary wave mechanism, the lowering of ice sheets induces an anomalous stationary wave train along the westerly waveguide that propagates into the EASM region, generating an equivalent-barotropic low response; this leads to reduced lower-tropospheric southerlies, which in turn reduces the dry enthalpy advection into East Asia, and hence the EASM precipitation.
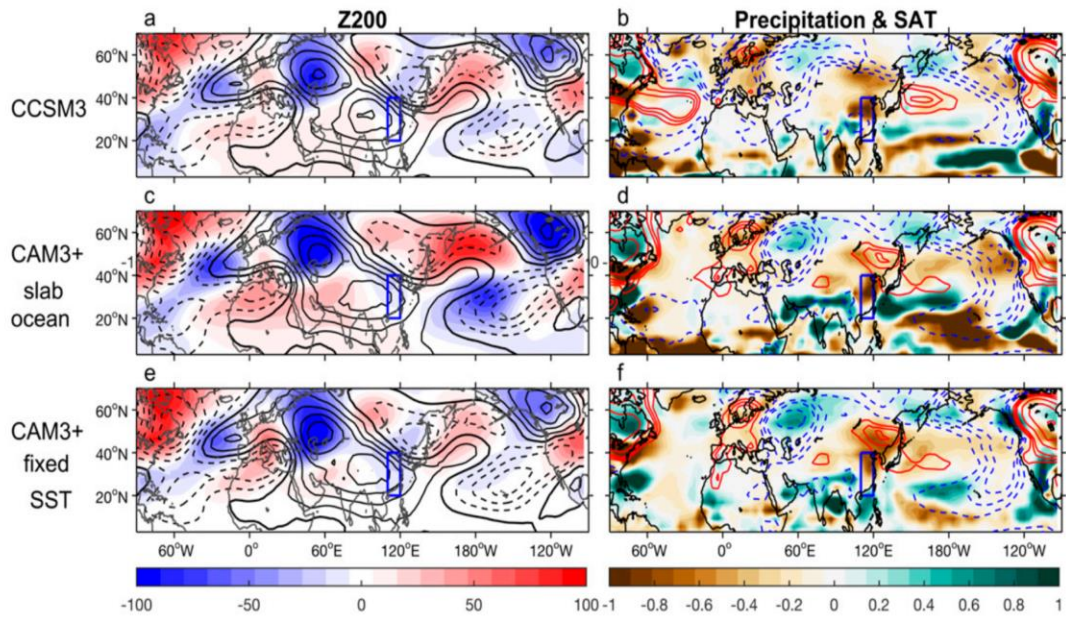
Figure 1. Anomalies induced by reduced NH ice sheet thickness in summer in (a),(b) fully coupled experiments (0% minus 100%), (c),(d) SLAB experiments [(0L+0E) minus (100L+100E)], and (e),(f) AGCM experiments [(0L+0E_AGCM) minus (100L+100E_AGCM)] for the following atmospheric variables in JJA: (left) eddy geopotential height at 200 hPa (Z200; shading; gpm) and (right) precipitation (shading; mm day^{-1}) and surface air temperature (SAT; contours; K). Contours in (a), (c), and (e) represent Z200 climatology at LGM in corresponding models; contour intervals are 30 gpm; dashed contours indicate negative values. In (b), (d), and (f), red solid contours are for SAT anomalies of 1, 2, 3, 6, 10, and 15 K, indicating warming anomalies; blue dashed contours are for SAT anomalies -1, -2, -3, -6, -10, and -15 K, indicating cooling anomalies. The model domains for calculating the EASM meridional wind index at 850 hPa (110° - 120° E, 20° - 40° N) are represented in the blue boxes.
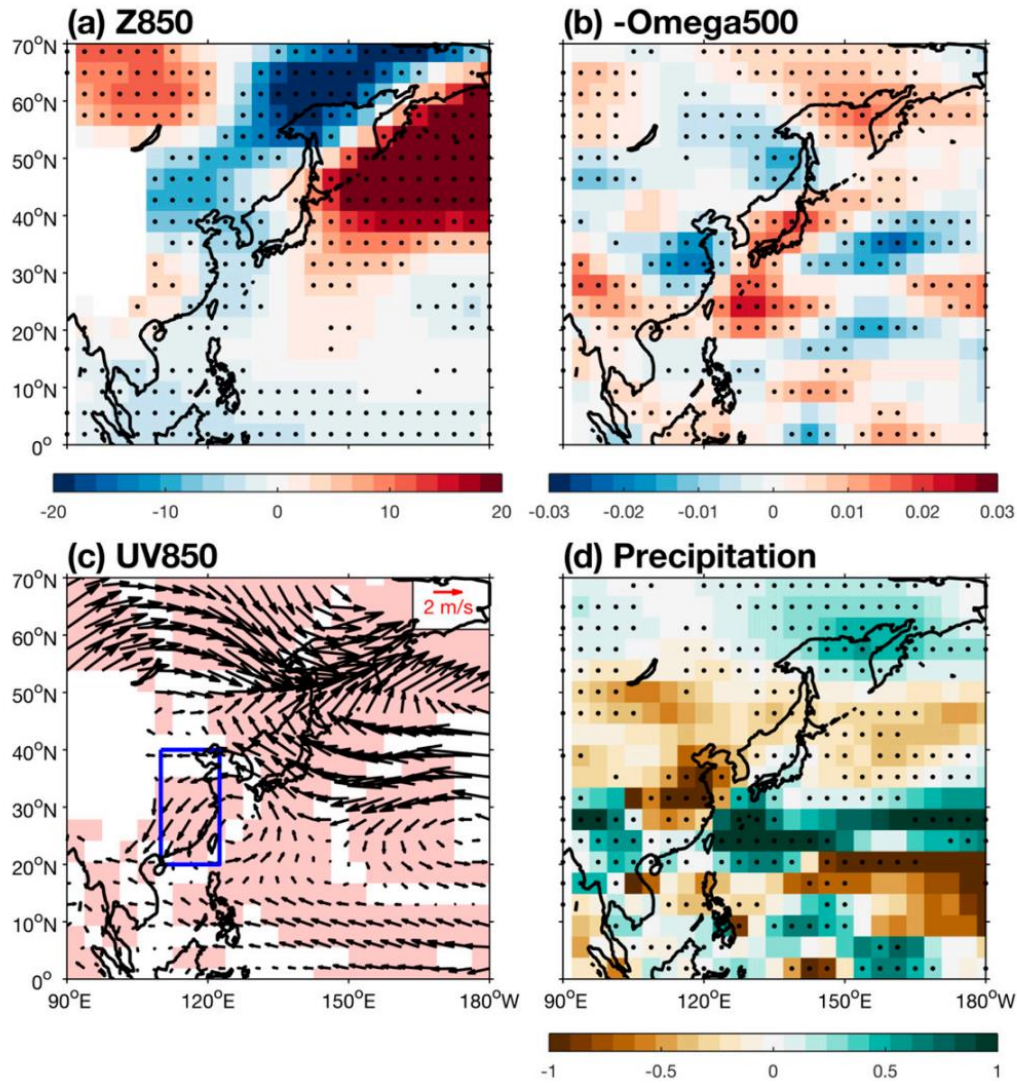
27

Figure 2. Atmospheric anomalies induced by reduced NH ice sheet thickness [experiment (0L+0E) minus (100L+100E)] over East Asia in summer for (a) eddy geopotential height (gpm) at 850 hPa; (b) vertical velocity $-\omega$(Pa s^{-1}) at 500 hPa; (c) wind (vectors; m s^{-1}) at 850 hPa; (d) precipitation (shading; mm day^{-1}). The model domain for calculating the EASM meridional wind index at 850 hPa (110° – 120° E, 20° – 40° N) is represented by the blue box in (c). Pink shadings and black dots represent anomalies that are statistically significant at a 95% confidence level.

9. 更新世赤道太平洋铁输入与蛋白石沉积的联系

翻译人：王敦繁 dunfan-w@foxmail.com

摘要：海洋初级生产力和输出量在海洋中高营养、低叶绿素地区增长，特别是在干燥和风尘增多的冰期，被认为与铁的输入增强有关。在现代海洋中，铁的输入十分重要，因为它限制了高营养、低叶绿素区域的生产量。但在在低营养环境中可能也是如此。我们的研究评估了过去数百万年赤道太平洋高营养、低叶绿素区域的沉积记录中的生产力与铁的关系。我们发现铁输入、生物硅(蛋白石)的产出和埋藏总产量之间存在着密切的联系。我们的数据表明，铁输入与蛋白石积累的关系比其他任何生物成分都更密切，高铁输入与大量增加的蛋白石沉积有关。铁和硅的现代生物地球化学行为，以及硅藻群落对它们相互作用的响应，与一百万年来铁和蛋白石积累之间的密切联系是一致的。我们的数据验证了早期关于铁在地质时间尺度上的生物效应的观点。

ABSTRACT: Increases in overall marine primary productivity and export production in high-nutrient, low-chlorophyll regions of the ocean have, particularly during dry and dusty glacial periods, been hypothesized to be linked to the enhanced delivery of iron. In the modern ocean, iron availability limits production in high-nutrient, low-chlorophyll regions, and may be important in lower-nutrient settings as well. Here, we assess the relationship between productivity and iron in sedimentary records from the high-nutrient, low chlorophyll region of the equatorial Pacific Ocean over the past million years. We find strong links between iron input, the export and burial of biogenic silica (opal) and total export production. Our data demonstrate that iron accumulation was more closely tied to the accumulation of opal than any other biogenic component, with high iron input associated with substantially increased opal sedimentation. The strong links between iron and opal accumulation over the past one million years are in agreement with the modern biogeochemical behaviour of iron and silica, and the response of the diatom community to their mutual availablity.

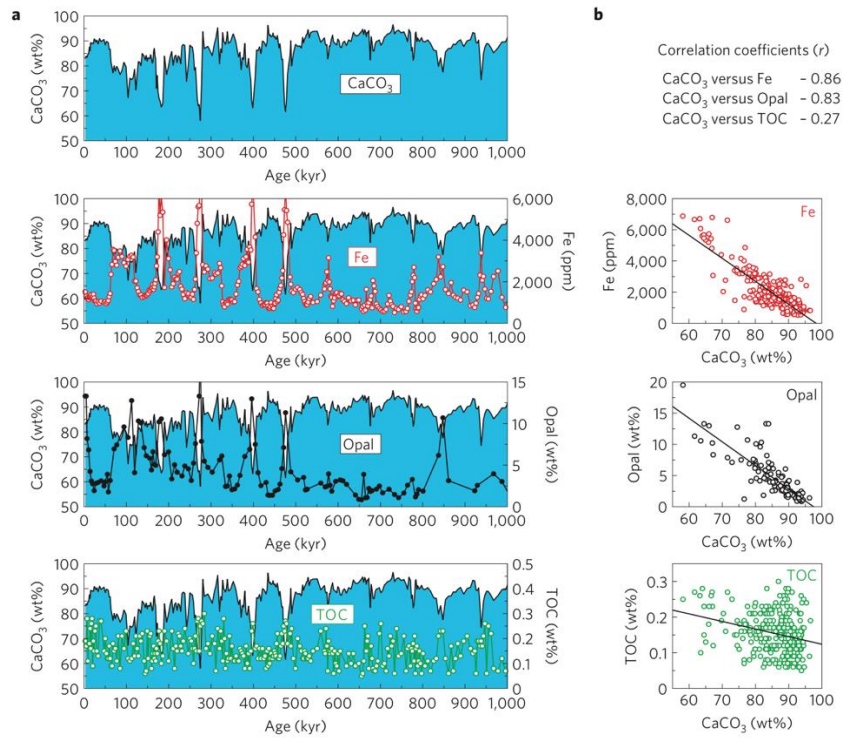our data support earlier suggestions of a biological response to iron delivery over geologic timescales.

Figure1. Concentrations of the biogenic components and Fe in core PC72. a, Time series of CaCO3 (wt%), Fe (ppm), biogenic opal (wt%) and TOC (wt%), plotted versus age (in kyr). b, Correlations between CaCO3 and the components shown in a, with (r) as shown. All p < 0.001.

10. 利用 XRF 扫描结果评估 Zr / Rb 作为南大洋冰河沉积物粒度变化的指标

翻译人：王浩森 502691781@qq.com

摘要：从 X 射线（XRF）得到的（Zr / Rb）比值具有作为高分辨率示踪剂的潜力，可用于冰川海洋沉积物的粒度变化。为了评估这种方法，我们对来自南大洋不同地区的一系列沉积物进行了高分辨率的粒度测量，以及通过 XRF 扫描和电感耦合等离子体质谱法（ICP-MS）进行 Rb 和 Zr 的测量。我们发现，尽管由于样品和其他因素的影响，Rb 和 Zr 计数与浓度显着偏离，但 XRF 得到的 Zr / Rb 比值与 ICP-MS 分析得到的结果是一致的。Zr / Rb 比值显示与总体平均粒度的差异能够很好的相关，但与不包括未分类的粗沉积物组分的平均粒度（即 IRD 校正的平均粒度）。这些观察结果得到了粒度分离实验的证据支持，该实验表明 Zr 和 Rb 集中在不同的粒度部分中。 ln（Zr / Rb）比值对粗粒度缺乏敏感性，因此记录的趋势与可分类粉尘百分比（SS％）和可分类粉尘平均值（SSM）晶粒大小相似。 ln（Zr / Rb）与 SS％（34.1）以及 ln（Zr / Rb）与 SSM（12.7）的关系图中存在通用梯度，因此 ln（Zr / Rb）比值提供了一种方便的方法估算 SS％和 SSM 的变化。总的来说，我们的结果支持使用 ln（Zr / Rb）比值作为沉积物分流情况下底部水流强度的指标。

ABSTRACT: The ln(Zr/Rb) count ratio derived from X-ray fluorescence (XRF) core scanning holds potential as a high-resolution tracer for grain-size variations of glaciomarine sediments. To evaluate this approach, we conducted high-resolution grain-size measurements, together with Rb and Zr measurements by XRF core scanning and Inductively Coupled Plasma-Mass Spectrometry (ICP-MS), on a series of sediment cores from different regions of the Southern Ocean. We find that downcore changes of the ln(Zr/Rb) count ratio from XRF core scanning are consistent with Zr/Rb concentration ratios derived from ICP-MS analyses, even though Rb and Zr counts deviate significantly from concentrations due to specimen and matrix effects. The ln(Zr/Rb) count ratio displays discrepancies with the bulk mean grain-size, but correlates well with the mean grain-size

of the sediment fractions that do not include unsorted coarse IRD (i.e. IRD-corrected mean grain-size). These observations are supported by evidence from a grain-size separation experiment, which indicates that Zr and Rb are concentrated in different grain-size fractions. Consistent with its lack of sensitivity to coarse grain-size fractions, the ln(Zr/Rb) ratio records similar trends to the sortable silt percent (SS%) and sortable silt mean (SSM) grain-size. Universal gradients exist in plots of ln(Zr/Rb) versus SS% (34.1), and ln(Zr/Rb) versus SSM (12.7), such that the ln(Zr/Rb) ratio provides a convenient way to estimate the magnitude of changes in SS% and SSM. Overall, our results support the use of the ln(Zr/Rb) ratio as an indicator of bottom current strength in cases where the sediment is current-sorted.
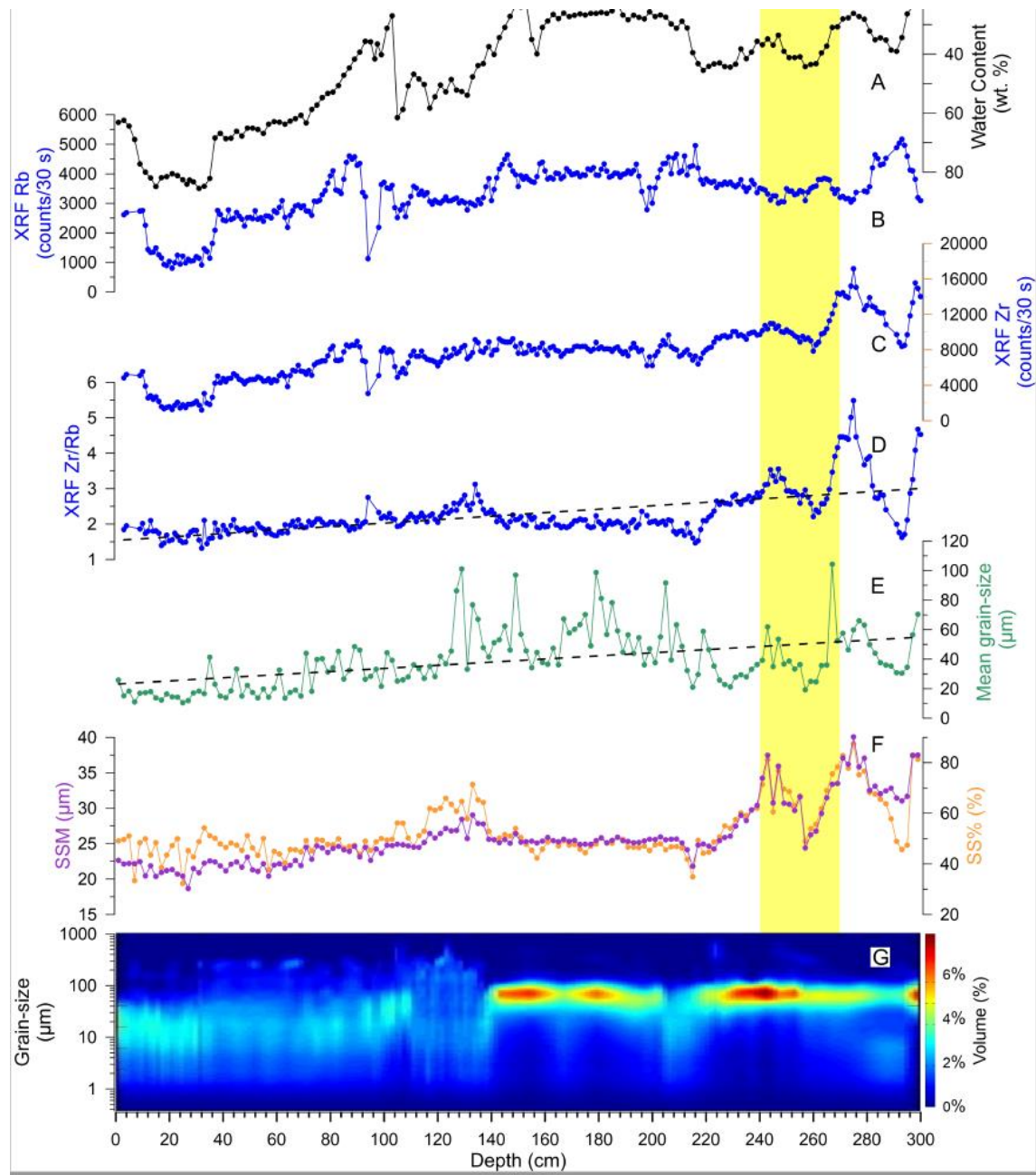
Fig. 1 Downcore records from Ross Sea core JB06 plotted versus depth. (A) Water content (note reversed axis). (B) Rb counts from XRF scanning. (C) Zr counts from XRF scanning. (D) Zr/Rb count ratio from XRF scanning. (E) Mean grain-size. (F) SSM and SS%. (G) Spectrum of grain-size compositions. Dashed lines in (D) and (E) indicate the general decreasing trends towards the core top. The yellow shading indicates a layer rich in benthic foraminifera ESSOAr |

Cassidulina sp. of last glacial age (< 1160 36 ka ^{14}C age according to Taviani et al. 1161 (1993) and Yokoyama et al. (2016)).

11. 马达加斯加西北部石笋 4000 年的多指标记录对气候变化、人类对环境的影响和巨型动物灭绝之间的关系的启示

翻译人：郑威　11930589@mail.sustech.edu.cn

摘要：来自马达加斯加西北部的Anjohibe洞的石笋ANJ94-2提供了一个非常详细的有精确定年的环境条件变化记录，再结合前人发表的石笋、湿地沉积物和考古遗址数据，可以洞悉过去气候变化、人类对环境的影响和巨型动物灭绝。石笋ANJ94-2的多指标记录有碳氧稳定同位素、矿物学分析（文石方和解石）、纹层交界面、层厚和碎屑物质。这些指标指示了自然环境对几十年到几百年尺度降雨变化的响应；与其他区域指标对比的结果显示马达加斯加西北部的湿润条件可能与北半球的变冷有关。碳同位素数据显示了该地区最大的环境变化的时间与大约1200年前人类的刀耕火种农业的出现吻合，这段时间没有干旱，湿润条件可能有轻微的增强。从石笋和湿地数据中显示出的1200到600年前的环境变化的时间点和程度指示了人类对地表的改造造成了马达加斯加的巨型动物灭绝。另一方面，结合其他最近的研究指示了干旱不是导致马达加斯加巨型动物灭绝的原因。

ABSTRACT：Stalagmite ANJ94-2 from Anjohibe Cave in northwestern Madagascar provides an exceptionally detailed and precisely dated record of changing environmental conditions that, combined with previously published data from stalagmites, wetland deposits, and archaeological sites, allows insights into past climate change, human environmental impact, and megafaunal extinction. Proxies of past conditions recovered from Stalagmite ANJ94-2 include ratios of carbon and oxygen stable isotopes ($\delta^{13}C$ and $\delta^{18}O$), mineralogy (calcite and aragonite), layer-bounding surfaces, layer-specific width, and detrital material. Those proxies suggest that the natural environment changed in response to changes in rainfall at time scales of a few decades to multiple centuries; comparison with distant proxies suggests that wetter conditions in northwestern

Madagascar may have been linked to cooling in the Northern Hemisphere. Carbon isotope data nonetheless suggest that the greatest environmental change in the area coincided with human introduction of swidden (*tavy*) agriculture about 1200 years ago, during a time not of drought but perhaps of slightly increasing wetness. The timing and extent of environmental change 1200 to 600 years ago seen in stalagmite and wetland data suggest that human modification of the landscape had a causal role in the extinction of Madagascar's megafauna. On the other hand, the results combine with other recent research to indicate that drought was not the cause of the megafaunal extinction.
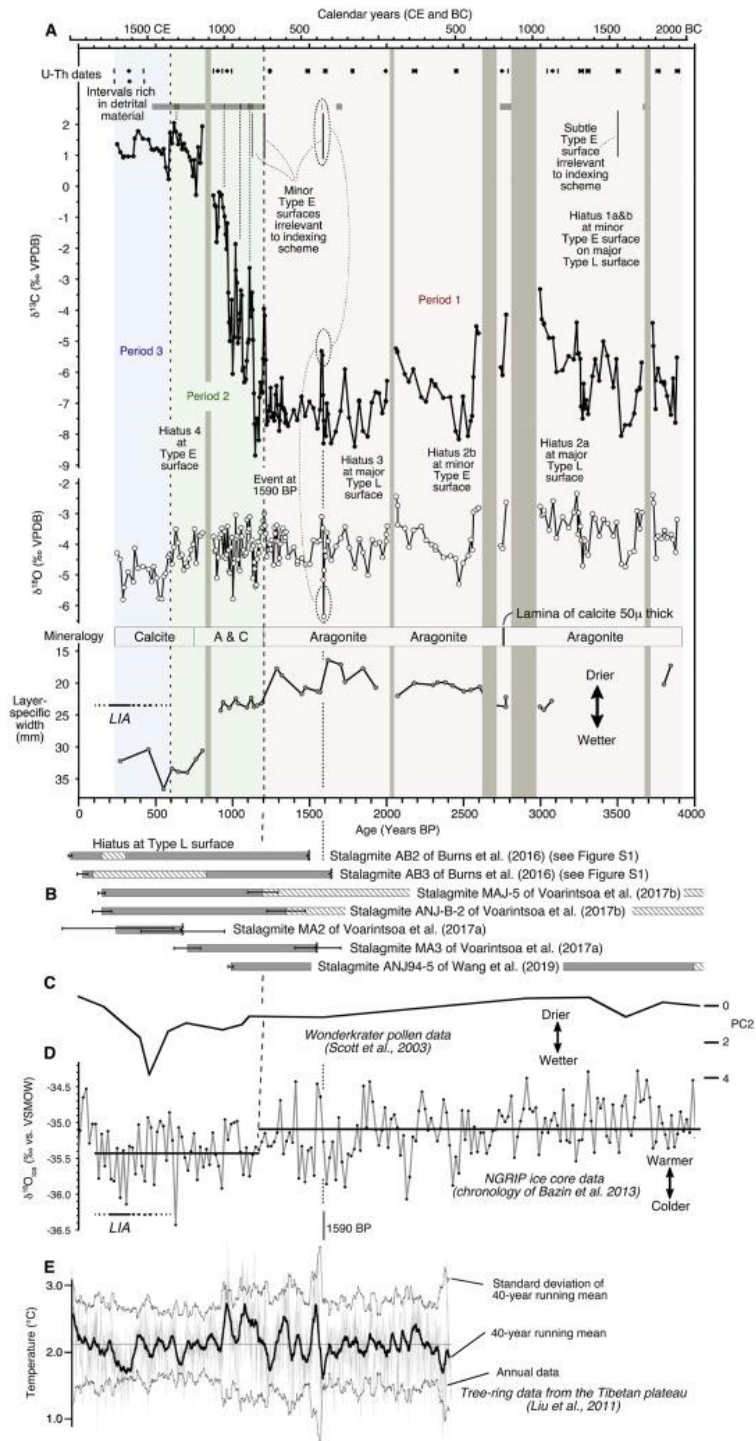
Figure 1. (A) Isotopic and petrographic data from Stalagmite ANJ94-2 from Anjohibe Cave in northwestern Madagascar; (B) age ranges of other stalagmites from northwestern Madagascar: (C) pollen data from South Africa; (D) ice-core data from Greenland; and (E) a tree-ring record of temperature from the Tibetan Plateau. Fig. 6 examines relationships within the stable isotope data, and Fig. 7 shows time-series of isotopic data during events at 1130 BP, 1580 BP, and 3250 BP in more detail.